A data-driven Bayesian optimisation framework for the design and stacking sequence selection of increased notched strength laminates

T.R.C. Chuaqui*[a], A.T. Rhead[a], R. Butler[a], C. Scarth[a]

[a] Materials and Structures Centre, Department of Mechanical Engineering, University of Bath, BA2 7AY Bath, UK

Abstract

A novel Bayesian optimisation framework is proposed for the design of stronger stacking sequences in composite laminates. The framework is the first to incorporate high-fidelity progressive damage finite element modelling in a data-driven optimisation methodology. Gaussian process regression is used as a surrogate for the finite element model, minimising the number of computationally expensive objective function evaluations. The case of open-hole tensile strength is investigated and used as an example problem, considering typical aerospace design constraints, such as in-plane stiffness, balance of plies and laminate symmetry about the mid-plane. The framework includes a methodology that applies the design constraints without jeopardizing surrogate model performance, ensuring that good feasible solutions are found. Three case studies are conducted, considering standard and non-standard angle laminates, and on-axis and misaligned loading, illustrating the benefits of the optimisation framework and its application as a general tool to efficiently establish aerospace design guidelines.

Keywords: B. Strength, B. Stress concentrations, C. Finite element analysis (FEA), C. Damage mechanics, Optimisation

1. Introduction

Composite materials are increasingly used in the aerospace industry due to their favourable specific strength and stiffness, and their anisotropic behaviour, which allows for efficient tailoring of the design variables to meet particular performance requirements. However, this increased flexibility comes at a cost, with design variables spanning not only the properties of the material, its constituents and their volume fractions, but also the combination of ply angles and their stacking sequence, making laminate optimisation particularly challenging. Thus, the numerical or analytical evaluation of the performance requirements must be computationally inexpensive, especially when using global optimisation methods, such as genetic algorithms or particle swarm methods, which require an extensive number of objective function evaluations. In the context of composite structures, such methods are usually limited to optimisation of quantities which are relatively inexpensive to compute, such as in-plane properties, flexural rigidity, maximum buckling load and maximum natural frequencies [1, 2].

For other performance characteristics, such as laminate strength under three-dimensional stress states, inexpensive solutions are often unavailable. First-ply failure criteria based on classical laminate theory (CLT) and simple shell/plate formulations can be used in limited cases, such as dispersed laminates employing the $0°$, $\pm 45°$ and $90°$ standard angles (SAs), where failure is brittle and dominated by in-plane fibre stresses. These simple methods are, however, unable to predict the behaviour of a wide range of unconventional laminates, where resin-dominated damage mechanisms can evolve sub-critically leading to more progressive failure. Examples of unconventional designs range from laminates employing non-standard angles (NSAs, i.e angles other than SAs), which may offer significant benefits in production efficiency and formability [3–5], to laminates employing thick ply blocks (as opposed to dispersed laminates), which can delay ultimate failure near stress raisers [6, 7]. Predicting the strength of such designs typically requires complex three-dimensional progressive damage finite element (FE) models that account for the out-of-plane stresses, non-linear shear behaviour and the different interacting failure modes. The computational expense associated with these models renders global optimisation methods intractable, and thus, optimising for laminate strength in this broad design space is still largely unexplored.

Alternatively, rather than optimising the objective function directly, a surrogate of the FE model can be used instead to guide the search of optimisation and minimise the number of FE evaluations. This surrogate must be inexpensive to evaluate so that it can provide estimates of the FE solutions across the entire design space in an efficient manner. The use of probabilistic surrogate models provides not only predictions of objective functions, but also of uncertainty in these predictions. The use of such a model enables the objective function to be evaluated using the complex FE model at design points where sampling is more likely to yield an improvement. These approaches are generically designated by *data-driven* or *efficient* global optimisation methods. One popular method is Bayesian optimisation, which is derivative-free, facilitates global optimisation and has been shown to require fewer evaluations than both genetic algorithms and particle swarm methods [8]. Therefore, Bayesian optimisation is often used in black-box problems where it is desirable to minimise the number of objective function evaluations due to their costly computation, or in experimental settings when tests are expensive and time-consuming. Examples of application range from hyperparameter tuning in classic machine learning algorithms and deep neural networks [9–12], reinforcement learning [13], robotics [14, 15], environmental monitoring [16], materials discovery [17] and pharmaceutical product development [18]. The interested reader is referred to [19] for a comprehensive review of the method and its applications.

Bayesian optimisation has also been increasingly used in the design of composite structures. In particular, Bayesian machine learning and optimisation were used in [20] for the design of ultra-thin composite shell structures in the post-buckling range. Bayesian optimisation has also been applied for improved buckling performance of variable stiffness composite plates and cylinders [21–23] and of curved fibre composite panels with cut-outs [24]. Other notable applications include optimisation

of composite wind turbine blades for lightning strike and multi-axial fatigue loading [25] and optimisation of sandwich composite armour design for blast mitigation [26]. Bayesian optimisation has also been applied in the design of aligned discontinuous composites considering a variety of performance characteristics [27] and in the multi-objective design of parts containing ply-drops, where stiffness, Tsai-Wu omni-strain failure criterion and manufacturing time requirements were considered [8]. Other similar surrogate-based optimisation strategies have also been developed for buckling of variable stiffness composites under buckling [28, 29] and in the design of filament-wound cylindrical shells with variable angle tow [30]. However, the method has not been applied to strength optimisation of multi-directional laminates considering the interaction and progression of the different damage mechanisms associated with their failure.

In this paper, a novel Bayesian optimisation framework of lay-up configuration of multi-directional composite laminates is proposed for structural strength. To the authors' knowledge, the framework is the first to combine high-fidelity progressive damage FE modelling with a data-driven optimisation methodology for strength of composite laminates. The framework includes a bespoke and novel methodology for incorporating constraints within Bayesian optimisation, which is used to enforce common aerospace design requirements, such as specified in-plane stiffness, symmetry about the laminate mid-plane and balance of plies. The methodology allows evaluation of infeasible points to improve the accuracy of the surrogate model but, as the optimisation progresses, gradually limits sampling to feasible regions only. The primary contribution of this paper is the development of an optimisation framework which can achieve very good laminate solutions in relatively few FE model evaluations, a necessary feature when optimising such complex models, whilst enforcing the strict constraints associated with industrial stacking sequence design.

The case of open-hole tensile (OHT) strength is chosen as a complex objective, which can display a variety of failure modes, requiring an expensive FE model for which Bayesian optimisation is particularly well suited. OHT is also an early indicator of structural strength and an important design allowable in the aerospace industry. However, the proposed framework is generic and can be applied to any composite structure under any loading condition. The framework is demonstrated in three case studies in which OHT strength is optimised subject to the aforementioned design requirements, and across design spaces comprising different combinations of standard and non-standard angle laminates, under both on-axis and misaligned loading. The progressive damage FE model originally presented in [7] is modified and used herein to demonstrate the proposed framework. An overview of the optimisation problem is provided in section 2, followed by details of the methodology in section 3 and the FE model, which is described in section 4. Results and discussion are presented in sections 5 and 6, respectively.

2. Optimisation problem

To showcase the framework, a common industrial design problem is considered, consisting of a 36×36 mm plate with a 6 mm central open-hole, manufactured from AS4/8552 pre-preg, and subjected to remote longitudinal tension. The plate is 3.9 mm thick, corresponding to a laminate with $N_p = 20$ plies. Due to the mid-plane symmetry requirement usually employed in the aerospace industry, the number of plies which may be varied independently in the optimisation problem reduces to 10. The problem is illustrated in Figure 1.

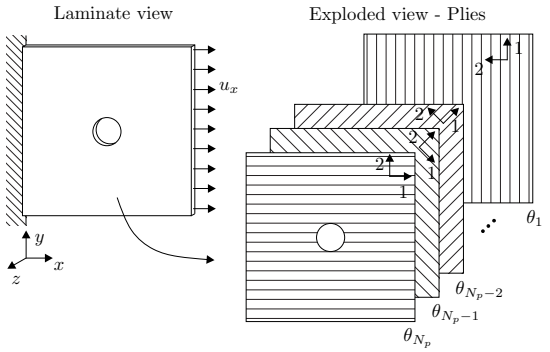

Figure 1: OHT laminate schematic. Applied displacement u_x. Global coordinate system (xyz) of the laminate and material coordinate system of the plies (123) are also shown.

The objective is to find the best possible stacking sequence, corresponding to the 10 ply angles, defined by a point in a 10-dimensional space $\mathbf{x} = \{\theta_1, ..., \theta_{10}\}$, that maximises the OHT strength of the laminate. This stacking sequence must also satisfy in-plane stiffness and balance of positive and negative ply angles, as aerospace components are not designed for just one performance characteristic. To achieve this, the strength is optimised assuming that stiffness design drivers have already been decided. In this problem, a 50/40/10 percent breakdown of $0°/\pm45°/90°$ plies, found in a typical wing skin, are considered, but any specified in-plane stiffness could be used. Prior to optimisation, different balanced, symmetric stacking sequences, employing both SA and NSA angles, are found by matching the specified in-plane stiffness using the strategy detailed in section 3.5.1. These design solutions constitute the feasible design space, where the optimal solution lies. Hence, for the sake of clarity, feasible points correspond to any solutions that satisfy the in-plane stiffness, balance and symmetry constraints, whereas infeasible points denote solutions that do not satisfy one or more constraints. Due to the heavily constrained design space, the Bayesian optimisation approach needs to be modified using a bespoke methodology, outlined in section 3.5, such that the application of these constraints does not compromise the effectiveness of the optimisation process. Note that the design constraints considered in this problem are only some of the requirements for aircraft structures, but they illustrate the proposed optimisation framework.

The design space is discretised with ply angles ranging between $-85°$ and $90°$ at a $5°$ increment. This discretisation is refined enough to capture the trends in OHT strength but large enough to be manufacturable, where manufacturing tolerances can be as high as $\pm3°$ for automated lay-up.

It also simplifies the optimisation process and allows for easier generation of the FE meshes.

Note that optimising for OHT strength considering the aforementioned design constraints does not necessarily lead to designs applicable to large real-world aerospace structures under a multitude of stress states and subject to several design constraints. The OHT example problem, however, serves as a practical demonstrator of the proposed optimisation framework. The framework is generic and can be easily adapted for other optimisation problems, allowing the introduction of other design constraints and easy modification of the objective function in order to optimise for other performance drivers.

3. Optimisation Methodology

3.1. Overview

The aim of Bayesian optimisation is to reach the best possible solution in the minimum number of evaluations of the objective function, which in this case correspond to expensive OHT strength predictions with the FE model. To achieve this, a probabilistic surrogate model of the objective function is created using Gaussian process (GP) regression [31]. A GP not only provides estimates of the trends in the observed data (GP mean), but it also provides estimates of uncertainty. These estimates are updated with new observed data, allowing the surrogate model to improve with more observations.

The Bayesian optimisation approach is illustrated in Figure 2 for a simple function, demonstrating convergence of the optimisation and increasing surrogate model accuracy across multiple iterations. The illustrated procedure is summarised as follows. First, a GP is fitted to some observed data points, corresponding to previous evaluations of the objective function, at iteration i in the optimisation process. The observed data used in this process is commonly referred to as *training* set (filled black circles on Figure 2). The GP is then used to make computationally inexpensive predictions of the objective function across the design space, at points where the value of the objective function is unknown. These predictions are defined by mean and uncertainty estimates (red curve and shaded red region on Figure 2), representing the predictions of the objective function value and the uncertainty (characterised by the standard deviation) in these predictions. The input points where the GP is evaluated constitute the *test* set.

The GP predictions are subsequently used to build an acquisition function (blue curve on Figure 2), which is responsible for the determination of the next best point to evaluate the objective function. The acquisition function computes a trade-off between *exploitation* and *exploration*. The former seeks to sample where the GP predicts high objective function values (high GP mean), thereby guiding the optimisation towards predicted optima, and the latter seeks to sample where GP uncertainty is high (high GP standard deviation), thereby improving surrogate model accuracy and potentially revealing hidden optima in previously unexplored regions of the design space. The objective function is subsequently evaluated at the input point that maximises the acquisition

function (denoted with a red triangle on Figure 2), which is more likely to yield an improvement of the objective whilst ensuring that the design space is adequately explored.

The new observation is appended to the training set and the process is repeated at iteration $i+1$, where the GP is re-fitted with the updated data. Note that the GP uncertainty now reduces to zero at the new observation. The process is repeated once again at $i+2$. It can be observed that as the optimisation algorithm progresses, the uncertainty in the surrogate model generally decreases and the predictions of the objective function become more accurate, directing the search towards the global maximum.

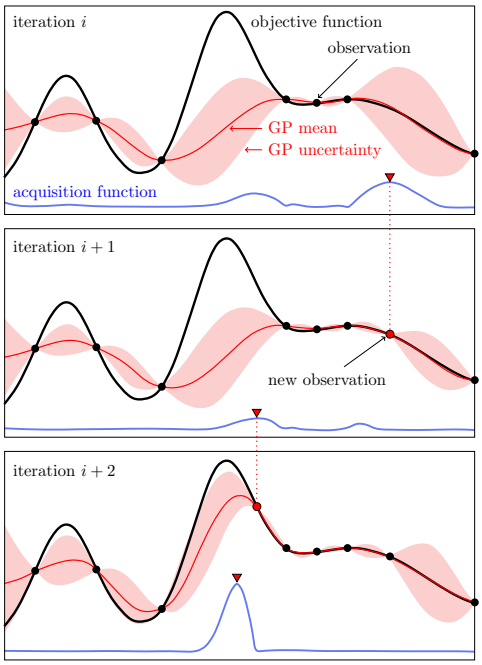

Figure 2: Bayesian optimisation schematic for three iterations. Training set corresponds to the set of observations, denoted by filled black circles. GP mean and uncertainty correspond to red curve and shaded red regions, respectively. Acquisition function corresponds to the blue curve and its maximum is marked with a red triangle.

With the Bayesian optimisation approach conceptually established, the actual implementation used in this work is now presented and follows the flowchart in Figure 3. The algorithm was fully automated and implemented in a bespoke Matlab script.

Prior to the optimisation process, an initial training set $\mathcal{T}_r^0 = \{\mathbf{X}, \mathbf{f}\}$ is constructed by sampling M points $\mathbf{X} = \{\mathbf{x}_1, ..., \mathbf{x}_M\}^T$ and evaluating the corresponding OHT strengths $\mathbf{f} = f(\mathbf{X})$ using the FE model. $\mathbf{X}$ is a $M \times (N_p/2)$ matrix, with each row corresponding to a stacking sequence and each column corresponding to a ply angle, and $\mathbf{f}$ is a $M \times 1$ column vector. The generation of the initial training set is described in detail in section 3.2. The optimisation routine is then initialised and repeated for $i = 1, ..., N$ iterations, where N is a user-defined limit. The training set from the previous iteration $\mathcal{T}_r^{i-1}$ is used to fit the GP, which is then used to make predictions on the test set $\mathcal{T}_e^i$ at each iteration i. Details on the GP and specific settings used in this work are given in section 3.3. The acquisition function is generated using the predictions on $\mathcal{T}_e^i$ and the stacking

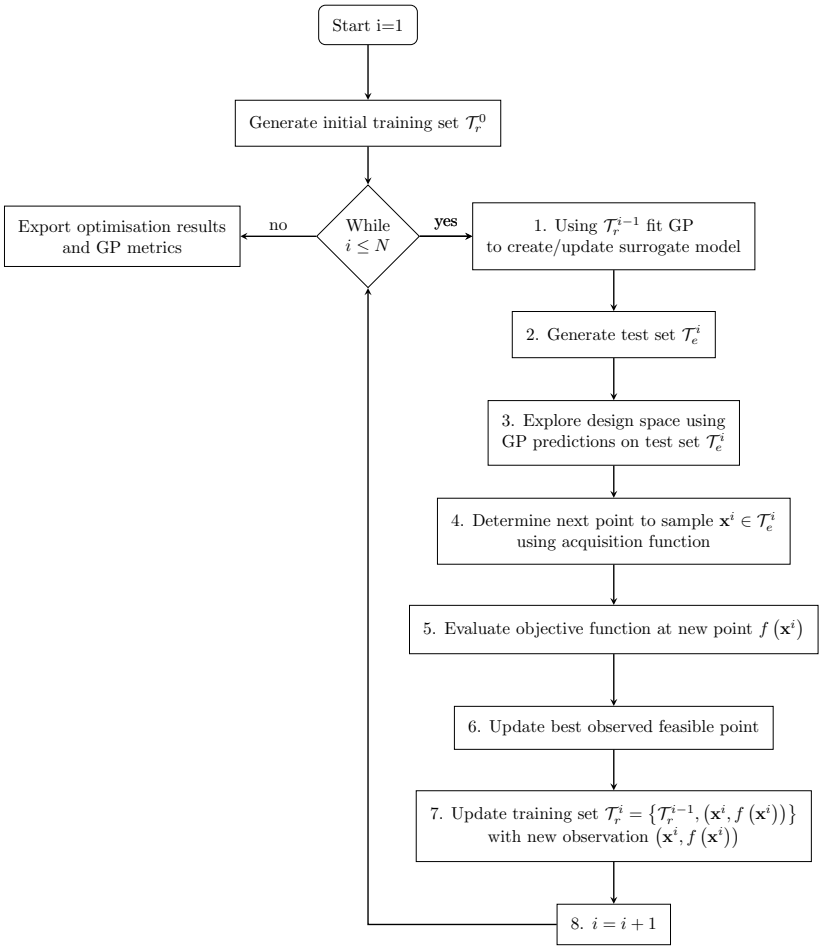

Figure 3: Flowchart of Bayesian optimisation algorithm.

sequence $\mathbf{x}^i$ that maximises its value is determined. Details on the choice of acquisition function are provided in section 3.4. The OHT strength of stacking sequence $\mathbf{x}^i$ is subsequently evaluated using the FE model. The best observed feasible point is then updated in case the newly evaluated stacking sequence fulfils all the constraints and displays higher strength. Lastly, the training set is updated with the newly evaluated point.

Because all possible stacking sequence candidates for OHT strength evaluation with the FE model are contained in the test set $\mathcal{T}_e^i$ at each iteration, it is important that this set meets two conditions: (i) it must be large enough and space-filling so that it allows the algorithm to adequately explore the design space and improve the surrogate model, in order to provide a better global approximation of the trends in OHT strength; (ii) it must contain potential new feasible optima that fulfil all the design requirements, corresponding, in practice, to the enforcement of the constraints on the design space, as described in section 2. To achieve this, the bespoke methodology in section 3.5 is proposed for the generation of $\mathcal{T}_e^i$ at every iteration i. This methodology is one of the major novel aspects of this work, and is ultimately a method for applying constraints within Bayesian optimisation without compromising GP accuracy, which would jeopardize the optimisation process.

3.2. Initial training set

Achieving a space-filling initial training set improves surrogate model performance, increasing the likelihood of finding optimal solutions in the optimisation process. Therefore, the initial training set $\mathcal{T}_r^0$ is generated using a Maximin Latin-Hypercube Sampling (MMLHS) algorithm [32], which optimises the space-filling properties of the set by maximising the minimum Euclidean distance between the M sampled points. The OHT strength of each randomly sampled point is subsequently evaluated using the FE model.

3.3. Gaussian process surrogate

Given a set of observations $\mathbf{f}$ at inputs $\mathbf{X}$ from the training set, the GP can be used to make predictions of the real objective function f at inputs $\mathbf{X}_*$ contained in the test set. The joint distribution of $\mathbf{f}$ with the predictions $\mathbf{f}_*$ follow a multivariate Gaussian distribution which, as shown in [31], can be partitioned into:

$$\begin{bmatrix} \mathbf{f} \\ \mathbf{f}_* \end{bmatrix} \sim \mathcal{N}\left(\begin{bmatrix} m(\mathbf{X}) \\ m(\mathbf{X}_*) \end{bmatrix}, \begin{bmatrix} \mathbf{K} + \sigma_n^2 \mathbf{I} & \mathbf{K}_* \\ \mathbf{K}_*^T & \mathbf{K}_{**} \end{bmatrix} \right) \tag{1}$$

where $\mathbf{K} = k(\mathbf{X}, \mathbf{X})$, $\mathbf{K}_* = k(\mathbf{X}, \mathbf{X}_*)$ and $\mathbf{K}_{**} = k(\mathbf{X}_*, \mathbf{X}_*)$. Functions $m(\mathbf{x})$ and $k(\mathbf{x}_i, \mathbf{x}_j)$ represent the mean of the Gaussian process at point $\mathbf{x}$ and the covariance of any two points $\mathbf{x}_i$, $\mathbf{x}_j$, respectively. The covariance function between two points is computed in the 10-dimensional space using the Euclidean distance. Note that although observations $\mathbf{f}$ relate to deterministic FE strength solutions, a very small noise parameter $\sigma_n = 1 \times 10^{-6}$ is added to the covariance matrix to facilitate its factorisation.

Using standard Gaussian conditioning rules, the GP predictions, given the training data and the inputs from the test set, follow a distribution with mean $\boldsymbol{\mu}_*$ and covariance $\boldsymbol{\Sigma}_*$:

$$\boldsymbol{\mu}_* = m(\mathbf{X}_*) + \mathbf{K}_*^T \left(\mathbf{K} + \sigma_n^2 \mathbf{I}\right)^{-1} (\mathbf{f} - m(\mathbf{X})) \tag{2a}$$

$$\boldsymbol{\Sigma}_* = \mathbf{K}_{**} - \mathbf{K}_*^T \left(\mathbf{K} + \sigma_n^2 \mathbf{I}\right)^{-1} \mathbf{K}_* \tag{2b}$$

The GP standard deviation can be computed trivially from $\boldsymbol{\Sigma}_*$. For the choice of the covariance function, the automatic relevance determination (ARD) Matérn 5/2 kernel was selected, after conducting a performance comparison against squared exponential, Matérn 5/2 and ARD squared exponential kernels. The mean $m(\mathbf{x})$ is parameterised solely in terms of the weight coefficients using constant explicit basis functions, which are set to one. The weights and kernel hyperparameters (signal standard deviation and characteristic length scales) are determined from maximisation of the marginal log likelihood using a quasi-Newton optimiser [33]. Note that maximisation of the marginal log likelihood can result in hyperparameters that correspond to local optima. Despite not being used here, a multi-start strategy could be included to prevent local optima and potentially boost GP performance. In addition, optimising the marginal log likelihood could lead to

overfitting in some instances. If this arises, the problem can be overcome using a fully Bayesian implementation, in which methods such as Markov Chain Monte Carlo (MCMC) [34] are used to sample from the posterior distribution of the hyperparameters [35]. The reader is referred to [31] for more details on Gaussian process regression and selection of covariance functions.

3.4. Acquisition function

For the acquisition function, the expected improvement function is used according to [36]. For any single input $\mathbf{x}_*$ in the test set, the expected improvement function at iteration i can be written in terms of the GP mean $\mu(\mathbf{x}_*)$ and standard deviation $\sigma(\mathbf{x}_*)$:

$$\mathrm{EI}^i(\mathbf{x}_*) = \begin{cases} [\Phi(Z)\, Z + \phi(Z)]\, \sigma(\mathbf{x}_*), \text{ if } \sigma(\mathbf{x}_*) > 0 \\ 0, \text{ if } \sigma(\mathbf{x}_*) = 0 \end{cases} \tag{3}$$

and

$$Z = \begin{cases} \left(\mu(\mathbf{x}_*) - f\left(\mathbf{x}_+^{i-1}\right) - \xi^{exp}\right)/\sigma(\mathbf{x}_*), \text{ if } \sigma(\mathbf{x}_*) > 0 \\ 0, \text{ if } \sigma(\mathbf{x}_*) = 0 \end{cases} \tag{4}$$

where $f\left(\mathbf{x}_+^{i-1}\right)$ and $\mathbf{x}_+^{i-1}$ are the maximum observed feasible OHT strength and its corresponding stacking sequence, respectively, at iteration $i-1$. The terms Φ and ϕ correspond to the cumulative distribution function (CDF) and the probability density function (PDF) of the standard normal distribution, respectively. The exploration parameter ξ^{exp} is a user-defined positive real, proportional to the amount of exploration during the optimisation process. In this work, ξ^{exp} is set to a default value of 0.01 in every optimisation run.

3.5. Application of constraints

3.5.1. In-plane stiffness matching

The optimisation is subject to an equality constraint, which ensures that the in-plane laminate stiffnesses match prescribed target values, corresponding to specified percentages of standard ply angles, namely 0°, ±45°, and 90°. This constraint is implemented by finding combinations of non-standard ply angles which match this in-plane stiffness prior to the optimisation. In a given iteration of the optimisation, the test set, from which candidate designs are chosen, is subsequently populated with random permutations of these non-standard angles, as described in section 3.5.2.

Rather than directly matching stiffness terms, it is more straightforward to match in-plane lamination parameters, ξ_1 and ξ_2, defined as [37, 38]:

$$\xi_1 = \frac{1}{T}\int_0^T \cos(2\theta(z))\,\mathrm{d}z = \frac{1}{T}\sum_{l=1}^{N_p} \cos(2\theta_l)\, t_l \tag{5}$$

$$\xi_2 = \frac{1}{T}\int_0^T \cos(4\theta(z))\,\mathrm{d}z = \frac{1}{T}\sum_{l=1}^{N_p} \cos(4\theta_l)\, t_l \tag{6}$$

where T is the laminate thickness, θ_l and t_l denote the orientation and thickness of the l^{th} ply respectively, and N_p is the total number of plies. In-plane laminate stiffnesses A_{11}, A_{12}, A_{22} and A_{66} all have linear dependency upon ξ_1 and ξ_2 [38], and extension-shear coupling terms A_{16} and A_{26} are automatically zero for balanced laminates.

Suppose the stacking sequence is parameterised as a function of $N_p/4$ ply orientations, $[\pm\theta_1/\pm\theta_2/\ldots/\pm\theta_{N_p/4}]_{\text{S}}$, where N_p must be a multiple of 4 to ensure balance and symmetry are satisfied. Monte Carlo simulation may be used to identify combinations of the ply angles which result in lamination parameters within a user-defined tolerance from the target lamination parameters, that define the specified in-plane stiffness. The ply orientations, θ_l, are each allowed to take values from the discretised design space covering the interval $[-85°, 90°]$ at $5°$ increments. Realisations of candidate stacking sequences may be generated by sampling this discretised design space with uniform probability. For each sample realisation, the condition that the lamination parameters are sufficiently close to the target stacking sequence is stated as:

$$\sqrt{(\xi_1(\theta_1,\ldots,\theta_{N_p/4}) - \hat{\xi}_1)^2 + (\xi_2(\theta_1,\ldots,\theta_{N_p/4}) - \hat{\xi}_2)^2} \leq \epsilon_{\text{tol}} \tag{7}$$

where $\xi_{1,2}(\theta_1,\ldots,\theta_{N_p/4})$ denote the lamination parameters for a given set of ply orientations, $\hat{\xi}_{1,2}$ the target lamination parameters, and ϵ_{tol} is the acceptable tolerance upon the mismatch between the achieved lamination parameters and their target values. Using these components, the Monte Carlo method for in-plane stiffness matching may be summarised as:

1. Generate a large number of samples of $N_p/4$-dimensional discrete random variables, $\theta_1,\ldots,\theta_{N_p/4}$.
2. Calculate in-plane lamination parameters for each sample stacking sequence, $[\pm\theta_1/\pm\theta_2/\ldots/\pm\theta_{N_p/4}]_{\text{S}}$, using Eqs. (5-6).
3. Retain samples with lamination parameters within the acceptable tolerance of target lamination parameters in accordance with Eq. (7).
4. Isolate unique combinations of ply orientations from the remaining samples. Each combination corresponds to a vector $\mathbf{v}_j$, where $j = 1, ..., S$ and S is the number of feasible solutions found from the method.

It is emphasised that it is only unique combinations, and not permutations, which are retained in step 4, as the in-plane stiffness is unaffected by different permutations of the same combination of ply orientations. Although this stochastic methodology is not guaranteed to find all possible combinations of ply orientations which match the target lamination parameters, it becomes increasingly probable that all combinations will be found with an increasing number of samples. In practice, this method converges to a fixed number of solutions if a sufficiently large number of samples are used relative to the number of random variables, $N_p/4$. Due to the relatively low computation time required to compute lamination parameters using Eqs. (5-6), it is trivial to consider sample sizes in the order of 10^7 and return a set of stiffness-matched ply orientations

within seconds on a standard desktop PC.

3.5.2. Generation of feasible samples

In order to populate the test set at each iteration with feasible stacking sequences that match the target in-plane stiffness (within the prescribed tolerance), it is necessary to generate a set of F random permutations of the feasible combinations of ply orientations arising from the in-plane stiffness matching procedure described in section 3.5.1. This set of feasible points is defined as the feasible test set $\mathcal{T}_f^i$ and is used to generate the final test set $\mathcal{T}_e^i$, as described in the next section 3.5.3. A bespoke sampling approach is used to generate $\mathcal{T}_f^i$ at each iteration i, ensuring that the feasible design space is represented fairly and that the optimisation process is not excessively biased towards larger solution sets. The procedure follows:

1. For each unique angle combination $\mathbf{v}_j$, where $j = 1, ..., S$ and S is the number of solutions found from in-plane stiffness matching, generate a set $\mathbf{V}_j$ of size P_j containing all of its unique permutations.
2. Randomly sample F integers between $[1, S]$ with uniform probability.
3. Out of the F random integers, count the c_j number of repeats of each index j. c_j corresponds to the number of samples to draw from $\mathbf{V}_j$.
4. For each j, if $c_j > P_j$ then $c_{j,aux} = c_j$ and $c_j = P_j$. Repeat algorithm from item 3 with $F = c_{j,aux} - P_j$ and sampling between $[1, S] \setminus \{j\}$ until either $\sum_{j=1}^{S} c_j = F$ (number of desired samples is achieved) or $\sum_{j=1}^{S} c_j = \sum_{j=1}^{S} P_j$ (use all existing feasible solutions).
5. For each j, randomly sample c_j stacking sequences from the corresponding set $\mathbf{V}_j$, with uniform probability. The union of all sampled stacking sequences forms $\mathcal{T}_f^i$.

Note that this approach may need to be adapted in the case of laminates with a large number of plies, where generating all unique permutations can become computationally expensive. In such cases, a large user-defined set of randomly generated permutations can be used for each $\mathbf{V}_j$ instead.

3.5.3. Filtering strategy

The in-plane stiffness, balance and symmetry constraints result in very small feasible regions, which are not representative of the whole design space. Sampling points restricted to these regions only can lead to inaccurate surrogate models which do not capture the global trends in OHT strength, compromising the efficiency of the optimisation process. Therefore, to improve the surrogate model, the test set $\mathcal{T}_e^i$, and consequently the set of candidate points which may be added to the training set in the next iteration of the optimisation, must include space-filling samples across the entire design space. This idea is illustrated in an example in Figure 4 with a two-dimensional input space (as such, note that this Figure does not correspond to the real problem). First, in (i) a simple non-convex surface is used as an example of the objective function and the feasible regions are highlighted in red. The case of fitting a surrogate to feasible points only and the case

including infeasible points across the design space are illustrated in (ii) and (iii), respectively. Linear regression is used as a simple surrogate model for illustrative purposes. It can be observed in (ii) that the surrogate model is very flat and the global trend of the objective function is not captured, making it difficult to reach the optimum (corresponding to the maximum feasible point and highlighted with a green triangle). Including infeasible points in (iii) results in a better and more useful surrogate that can capture the global inclined trend, capable of guiding the optimisation towards better feasible points.

A novel methodology to enforce the design constraints without compromising GP accuracy is proposed. The methodology can be thought of as a filtering strategy, that applies the design constraints very gradually, and is illustrated in (iv) of Figure 4. In the early iterations of the optimisation process, the strategy aims at improving the accuracy of the GP and generates test sets $\mathcal{T}_e^i$ containing both feasible and infeasible points, spanning the entire design space. As the optimisation progresses, the number of infeasible points sampled in $\mathcal{T}_e^i$ is decreased, such that by iteration $i = i_{filter}$, the test set is composed of feasible points only and any stacking sequence chosen by the acquisition function lies within the feasible regions. At this stage, the GP is sufficiently accurate and the focus becomes optimising the solutions within the feasible regions. Note that other strategies for implementing constraints in a similar gradual manner could be to penalise the objective function evaluations associated with infeasible points by a coefficient with increasing magnitude over the course of optimisation. An alternative, but more elaborate method that generalises to a large number of complex, potentially computationally expensive constraints is to build the constraints into the acquisition function [39]. The proposed methodology is, however, a reasonable and practical approach when dealing with the inexpensive constraints associated with composite stacking sequence design rules, because the feasible design space is heavily constrained, corresponding to a relatively small number of discrete points, which are already known prior to optimisation.

For the implementation of the filtering strategy, the test set is defined as the union of a whole space test set, $\mathcal{T}_w^i$, containing infeasible points from the entire design space, and the feasible space test set $\mathcal{T}_f^i$ defined in section 3.5.2, containing points from the feasible regions only. The strategy is repeated at every iteration i and follows the steps:

1. Generate the feasible samples for $\mathcal{T}_f^i$, as described in section 3.5.2.
2. Sample $\mathcal{T}_w^i$ containing a large number of points $W = 10^5$ from the entire design space. Because the set has to be generated at every i, Latin-Hypercube Sampling (LHS) is used to minimise the computational cost compared with MMLHS (hence MMLHS is only used for the initial training set).
3. Determine the number R^i of infeasible points to remove from $\mathcal{T}_w^i$. A linear filtering function $L(i)$ is used such that $R^i = R^{i-1} + L(i)$. $L(i)$ increases linearly from 0 at $i = 1$ to $L(i) = W - R^{i-1}$ at $i = i_{filter}$. This ensures that at $i = i_{filter}$, all W points are removed

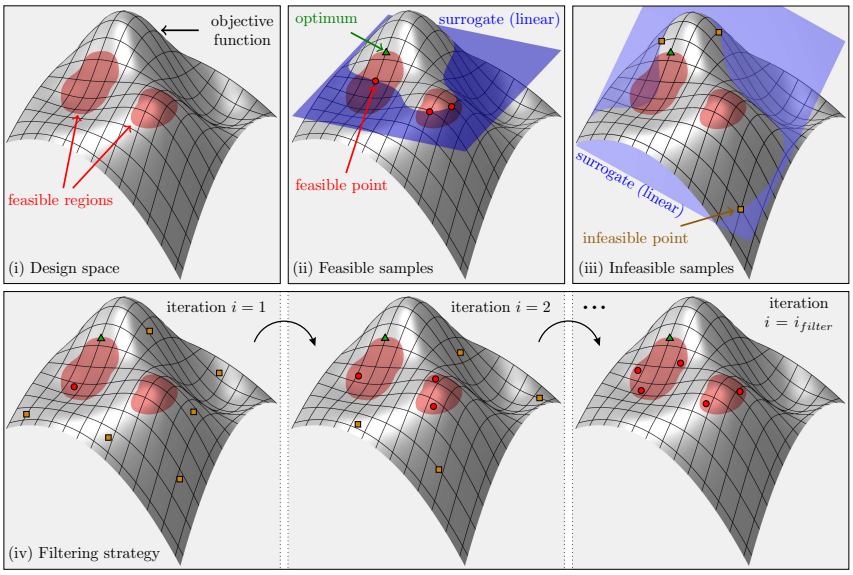

Figure 4: Effects of sampling from feasible regions only and from including infeasible points on surrogate model in (ii) and (iii), respectively. Illustration of the proposed filtering strategy in (iv). A simple non-convex surface and linear regression are used as examples of the objective function and of the surrogate model, respectively. The feasible regions are highlighted in red, as depicted in (i).

from $\mathcal{T}_w^i$.

4. The acquisition function is evaluated at all W points and the R^i lowest points are removed from $\mathcal{T}_w^i$.
5. The test set is formed $\mathcal{T}_e^i = \mathcal{T}_f^i \cup \mathcal{T}_w^i$.

4. Progressive damage finite element model

The optimisation script calls an external FE model, implemented in ABAQUS Explicit [40], to evaluate the objective function. A general overview of the implementation is shown in Figure 5.

The three-dimensional meso-scale FE model is based on the modelling framework proposed in [7]. The model includes a ply constitutive model based on continuum damage mechanics, an interlaminar model using frictionless surface-based cohesive zones and mesh alignment of the plies in their fibre direction. The model also includes an option that implements a numerical edge treatment which prevents premature failure in laminates prone to extensive free edge damage, thereby allowing simulations to attain 'more representative' open-hole strength, akin to a structure without the free edges. The numerical edge treatment follows the approach in [7] and consists of two 1 mm wide blocks, which are attached to each free edge of the specimen, using the same CFRP material but with no damage behaviour, effectively suppressing free edge effects. The approach is based on a resin edge treatment used in [41, 42] on experimentally tested coupons under 3-point and 4-point bending.

Unlike the original modelling framework in [7], the present model does not include any thermal analysis steps and the ply constitutive model has been modified (detailed in section 4.1) in order to

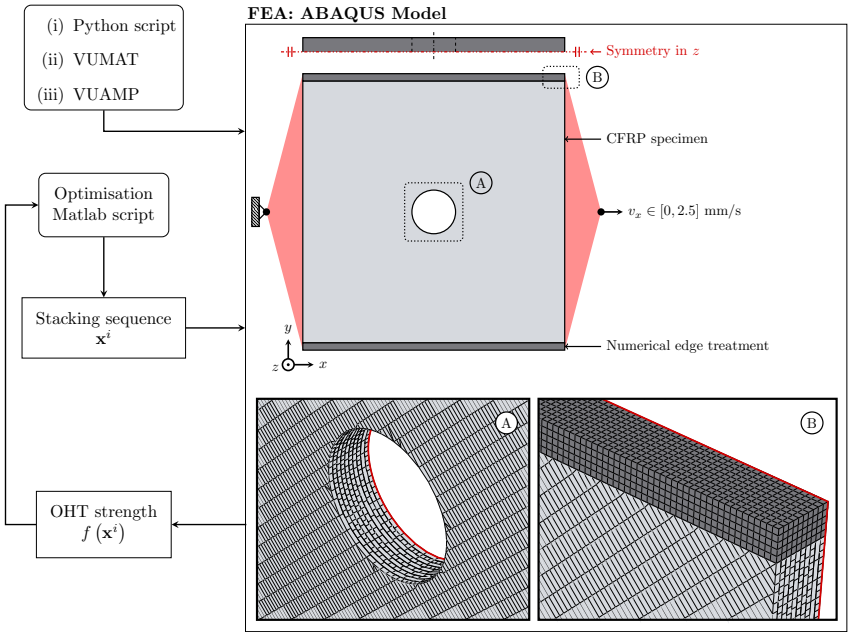

Figure 5: Implementation of objective function evaluation in the optimisation framework. Clamped and smooth-step velocity boundary conditions are applied. Symmetry boundary condition in z is applied at the mid-plane of the laminate. The ABAQUS model uses a bespoke Python script for mesh alignment, a VUMAT subroutine for the ply constitutive model and a VUAMP subroutine to halt the simulation after ultimate strength is reached.

reduce computation runtime and speed up the optimisation process. With the new modifications, runtime was substantially decreased, from approximately 7-12 hours to 20-50 minutes per simulation (variation dependent on lay-up configuration) when running with parallelisation on two Intel Ivybridge computing nodes with 2.6 GHz and 8 cores each. The reader is referred to the original article [7] for more details on the FE model parameters and for the AS4/8552 pre-preg material properties.

4.1. Ply constitutive model

In order to reduce computation runtime and enable a more tractable optimisation process, the ply constitutive model assumes that intralaminar failure occurs in fracture planes orthogonal to the ply orientation. Consequently, only in-plane stresses are affected by intralaminar damage. Damage associated with out-of-plane stresses is lumped at the ply interfaces and responsible for interlaminar failure only, following the approach in [43–46]. This simplification adequately captures OHT failure whilst enabling a significant reduction in computation runtime when compared to the original modelling framework in [7], where three-dimensional intralaminar damage and oblique fracture planes are considered. It should be noted that for other conditions such as transverse loading or compression, the fracture plane is generally oblique and the contribution of out-of-plane stresses to intralaminar failure is non-negligible. In such cases, this simplification may not be suitable and the consideration of oblique fracture planes and three-dimensional intralaminar damage modes, following formulations as per [7, 47, 48], is more appropriate. According to the plane-stress formulation in [43] and extending it to a three-dimensional stress state, the ply complementary

free energy density of a transversely isotropic ply, neglecting thermal and hygroscopic expansion, can be written as:

$$\begin{aligned}\mathcal{G} =& \frac{\sigma_{11}^2}{2\left(1-d_F\right)E_{11}} + \frac{1}{2E_{22}}\left(\frac{\sigma_{22}^2}{1-d_M} + \sigma_{33}^2\right) - \frac{\nu_{12}\left(\sigma_{22}+\sigma_{33}\right)\sigma_{11}}{E_{11}} - \frac{\nu_{23}\sigma_{22}\sigma_{33}}{E_{22}} \\ &+ \frac{\sigma_{12}^2}{2\left(1-d_M\right)G_{12}} + \frac{\sigma_{13}^2}{2G_{12}} + \frac{\sigma_{23}^2}{2G_{23}}\end{aligned} \tag{8}$$

The elastic strain tensor $\boldsymbol{\varepsilon}^e$ can be computed from the differentiation of the complementary free energy density with respect to the stress tensor $\boldsymbol{\sigma}$, resulting in:

$$\boldsymbol{\varepsilon}^e = \frac{\partial \mathcal{G}}{\partial \boldsymbol{\sigma}} = \mathbf{H} : \boldsymbol{\sigma} \tag{9}$$

where the colon operator denotes the double inner product and the fourth-order lamina compliance tensor $\mathbf{H}$, expressed in its matrix form, reads:

$$\mathbf{H} = \frac{\partial^2 \mathcal{G}}{\partial \boldsymbol{\sigma} \otimes \partial \boldsymbol{\sigma}} = \begin{bmatrix} \frac{1}{(1-d_F)E_{11}} & -\frac{\nu_{12}}{E_{11}} & -\frac{\nu_{12}}{E_{11}} & 0 & 0 & 0 \\ -\frac{\nu_{12}}{E_{11}} & \frac{1}{(1-d_M)E_{22}} & -\frac{\nu_{23}}{E_{22}} & 0 & 0 & 0 \\ -\frac{\nu_{12}}{E_{11}} & -\frac{\nu_{23}}{E_{22}} & \frac{1}{E_{22}} & 0 & 0 & 0 \\ 0 & 0 & 0 & \frac{1}{(1-d_M)G_{12}} & 0 & 0 \\ 0 & 0 & 0 & 0 & \frac{1}{G_{12}} & 0 \\ 0 & 0 & 0 & 0 & 0 & \frac{1}{G_{23}} \end{bmatrix} \tag{10}$$

where $\otimes$ denotes the tensor product. The total strain tensor is defined as the sum of the elastic and plastic terms $\boldsymbol{\varepsilon} = \boldsymbol{\varepsilon}^e + \boldsymbol{\varepsilon}^p$. Prior to damage initiation, the material response is linear elastic in longitudinal and transverse directions and non-linear elasto-plastic in shear, such that plastic strains ε_{ij}^p only exist for $i \neq j$. The non-linear plastic behaviour is described in each shear component using a uni-dimensional Ramberg-Osgood model [49, 50] and rate-independent isotropic hardening. d_F and d_M correspond to the damage variables for longitudinal and matrix failure, respectively. The variables evolve independently and irreversibly after damage onset in each respective mode such that d_F, $d_M \in [0, 1]$, with zero and one corresponding to undamaged and fully damaged material, respectively. Due to the significant difference in failure mechanisms, compressive and tensile longitudinal damage are tracked with independent auxiliary variables d_F^- and d_F^+. Therefore, in order to ensure closure of longitudinal cracks under load reversal, the total longitudinal damage variable d_F is defined as:

$$d_F = d_F^+ \frac{\langle \sigma_{11} \rangle}{|\sigma_{11}|} + d_F^- \frac{\langle -\sigma_{11} \rangle}{|\sigma_{11}|} \tag{11}$$

Considering an instant and increment in time t and Δt, the irreversibility of damage is enforced in both longitudinal and matrix failure modes considering:

$$d_k^{t+\Delta t} = \max\left\{0, \min\left\{1, \max\left\{d_k^t, d_k^{t+\Delta t}\right\}\right\}\right\} \ \forall\, t, \Delta t \geq 0,\ k = F, M \tag{12}$$

To determine the onset of damage, two sets of maximum strain criteria $\phi_F^+ \geq 1$ and $\phi_F^- \geq 1$ are used for longitudinal failure and a general in-plane quadratic stress criterion $\phi_M \geq 1$ is used for matrix failure:

$$\phi_F^+ = \frac{\varepsilon_{11} E_{11}}{X_T} \quad \text{if} \quad \varepsilon_{11} \geq 0 \tag{13a}$$

$$\phi_F^- = \frac{\varepsilon_{11} E_{11}}{X_C} \quad \text{if} \quad \varepsilon_{11} < 0 \tag{13b}$$

$$\phi_M = \left(\frac{\langle \sigma_{22} \rangle}{Y_T^{is}}\right)^2 + \left(\frac{\tau_{12}}{S_L^{is}}\right)^2 \tag{13c}$$

where X_T and X_C correspond to the uni-directional longitudinal tensile and compressive strengths and Y_T^{is} and S_L^{is} are the *in-situ* transverse tensile and longitudinal shear strengths, which can be calculated according to [51].

After onset, the same damages evolutions laws from [7] are used, and are illustrated in Figure 6 for each uniaxial material response. These include a coupled linear-exponential softening law for longitudinal tension, linear softening followed by constant stress kink-band broadening for longitudinal compression, and linear softening under mixed-mode conditions for matrix damage. Fully damaged elements are deleted according to the element deletion criteria in [52], preventing excessive distortion.

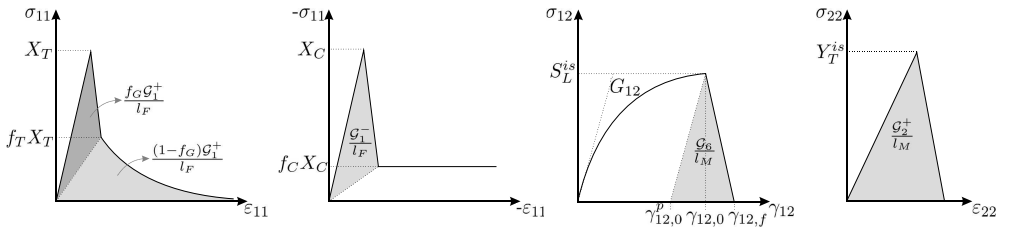

(a) 11 - Tension (b) 11 - Compression (c) 12 - Shear (d) 22 - Tension

Figure 6: Uniaxial material response under longitudinal tension, longitudinal compression, in-plane shear (with $\gamma_{12} = 2\varepsilon_{12}$) and transverse tension considered in the FE model. $\gamma_{12,0}^p$, $\gamma_{12,0}$, $\gamma_{12,f}$ correspond to plastic shear strain at onset of damage, total shear strain at onset of damage and final shear strain, respectively. $\mathcal{G}_1^+$, $\mathcal{G}_1^-$, $\mathcal{G}_2^+$ and $\mathcal{G}_6$ correspond to the critical fracture energies in longitudinal tension, longitudinal compression, transverse tension and shear, respectively. l_F and l_M are the characteristic finite element length and width, respectively.

4.2. FE model validation

The FE model was validated comparing the OHT strength predictions of 16 OHT laminates with the same aforementioned geometry, against the results from the experimentally-validated FE model proposed in [7]. The laminates are labelled according to their properties, which include: (i) standard-angle laminates (SA) or non-standard angle laminates (NSA); (ii) blocked stacking sequences, where plies with the same orientation are stacked together, and with a higher number corresponding to a more blocked laminate (e.g. SA6 is more blocked than SA3); (iii) imbalance of plies about the loading axis, introducing extension-shear coupling (e.g. laminates with a $+10°$ label, which correspond to the original versions rotated by $10°$). Different combinations of these

properties result in very different failure types, as discussed in [7], with more dispersed (less blocked) balanced laminates exhibiting more brittle failure, dominated by in-plane mechanisms. Conversely, blocked imbalanced laminates typically display extensive interlaminar and intralaminar matrix damage, resulting in more progressive failure. Validation of the model with this comprehensive set establishes confidence in its accuracy for a variety of laminates across the design space.

The relative trends in OHT strength from the present FE model and from [7] are shown in Figure 7. The results are plotted separately for SA and NSA laminates and from lowest to highest degree of ply blocking (SA3 to SA6 and NSA2 to NSA5, for SA and NSA cases, respectively). The cases with imbalance due to applied 10° rotation are also shown. The strengths are normalised by the SA6 laminate strength for each method (corresponding to the maximum observed value using both methods).

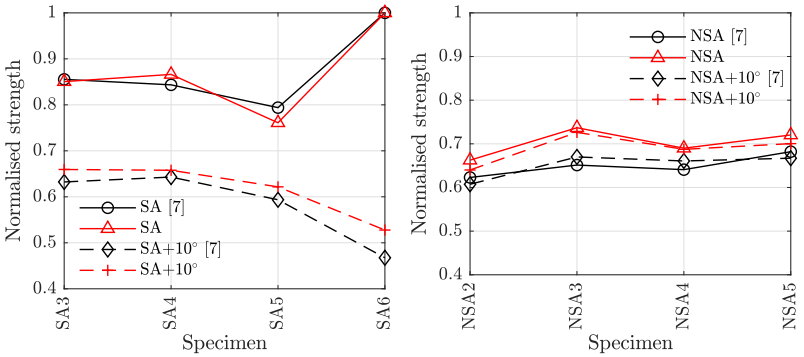

(a) SA laminates (b) NSA laminates

Figure 7: Comparison of relative trends in OHT strength from present FE model and from experimentally-validated FE model in [7], for both SA and NSA laminates, considering unrotated and rotated laminates (+10°), and from lowest to highest degree of ply blocking. Strengths are normalised by SA6 laminate strength for each method.

The relative trends in OHT strength are very similar using the present model and solutions from [7], as shown in Figure 7. Accurately predicting the relative trends in OHT strength with lay-up configuration is particularly important for the optimisation process, as these trends ultimately drive the optimisation towards the feasible optima. For completeness, note that the absolute values of OHT strength were also compared using the current FE model and [7], displaying a maximum difference of 15% and an average difference of 7.1% across the entire set.

5. Optimisation results

This section demonstrates the proposed optimisation process in three case studies. From case study I to case study II, the complexity of the optimisation process is increased due to an increased feasible design space. From case study II to case study III, optimisation complexity remains identical, but a more challenging loading condition is applied, which causes greater variability in strength and failure modes with changes in stacking sequence. The first and simplest case study corresponds to the optimisation of the laminate stacking sequence with feasible solutions

comprising SA laminates only, with 50/40/10 ply percentages. In case study II, the optimisation is run for feasible solutions including both SA and NSA stacking sequences, found from in-plane stiffness matching of the 50/40/10 ply percentages. Both case studies I and II are subject to on-axis loading, corresponding to the same problem but with different feasible design spaces. Lastly, case study III corresponds to optimisation of both SA and NSA, with the same feasible design space as case study II, but with a misaligned load. The results are discussed in section 6.

In both case studies I and II, two optimisation strategies are tested to demonstrate the benefits of the proposed filtering methodology: (i) A baseline optimisation with no filtering strategy where both training and test sets are composed of feasible points only. The initial training set is obtained with Maximin Sampling (MMS) from the feasible design space and the test set at each iteration corresponds to the feasible test set $\mathcal{T}_e^i = \mathcal{T}_f^i$. (ii) Optimisation with linear filtering strategy, where the training set and test sets include infeasible points and are generated according to sections 3.2, 3.5.3. The progression of the optimisation is analysed in terms of mean best feasible point and in terms of GP performance, using the mean relative error and mean standard deviation of the GP as performance metrics.

Due to the stochastic nature of the optimisation method, different results are expected across multiple runs. As such, in order to assess the robustness of the method, each optimisation case was run five times, for 100 iterations, with initial training sets of size $M = 15$, corresponding to a total of 115 FE evaluations, and with $i_{filter} = 25$ when employing the filtering methodology. The case studies also include a comparison of the mean best feasible solution from the optimisation runs against the mean best solution obtained from five runs of direct MMS of 115 points (identical number of FE evaluations) from the feasible design space. This comparison is used as a benchmark, in order to ascertain whether the Bayesian optimisation provides consistently better results than a random space-filling set of points. Note that for 10 optimisable ply angles, using a GA or a similar global optimisation method would generally require a large population size, of comparable magnitude to the total number of allowed FE evaluations, rendering these methods computationally intractable. For this reason, MMS is considered a more appropriate benchmark against which to compare the proposed methodology.

To compute the GP performance metrics, an external dataset comprising 500 points, sampled with MMLHS across the entire design space and evaluated with the FE model, was used. At each iteration of the optimisation process, the GP is used to make predictions of the expected value and standard deviations at each of these 500 points. The relative error of the GP is calculated at each point from the expected values and the FE model predictions. The mean relative error and mean standard deviation of all 500 points is subsequently computed. The 500-point external dataset is generated after all optimisation runs are completed, ensuring that none of the sampled points belong to the training data (including both initial training and new observations) used in any of the optimisation runs. This ensures that: (i) GP metrics are computed fairly and not validated on

training data; (ii) GP metrics of different optimisation runs can be compared as the same external dataset is used for their computation; (iii) the optimisation process is not restricted and any point with expected improvement can be sampled and subsequently used as training data.

It should be noted that because the objective of this work is to reach the best possible solution within a pre-defined maximum number of FE evaluations, no other stopping criteria are used. An alternative stopping criterion to extend the method and potentially reach a global optimum, if time is not a constraint, is to stop the optimisation if the change in the maximum value of the expected improvement function across the design space is below a specified minimum threshold over a given number of iterations. Such a criterion would indicate that further significant improvements in either the objective function, or in the accuracy of the surrogate, are unlikely.

5.1. Case study I: SA laminates only

Considering the 50/40/10 ply percentages of a wing skin, the feasible design space, containing SA stacking sequences only, comprises 7560 unique permutations. Because of the relatively small size of the feasible design space, the feasible test set at each iteration $\mathcal{T}_f^i$ is formed using all 7560 solutions.

Key performance metrics from this case study are shown in Figure 8. The comparison of the mean best feasible solution across the five repeat runs of each baseline and linear filtering optimisation strategies and from MMS is shown in Figure 8a. The evolution of the mean best feasible point, the mean GP relative error and the mean GP standard deviation are shown for both optimisation strategies in Figures 8b, 8c and 8d, respectively. Note that the mean GP relative error and mean GP standard deviation are taken across the 500-point external validation set. The standard deviations across the five repeat runs are shown along with the mean values in every plot.

The best feasible stacking sequence from each optimisation run is displayed in Table 1 along with its corresponding OHT strength. The iteration number at which the solution is found is also shown.

Table 1: Best feasible solutions for each optimisation run in case study I. Stacking sequence, OHT strength and corresponding iteration at which the best feasible solution is found are shown.

Optimisation strategy	**Run n°**	**Stacking sequence**	**OHT strength (MPa)**	**Iteration**
baseline	1	$[0_3/90/0_2/45/\text{-}45/45/\text{-}45]_S$	619.3	90
	2	$[0_3/45_2/\text{-}45_2/90/0_2]_S$	652.2	95
	3	$[0_3/45_2/\text{-}45_2/90/0_2]_S$	652.2	96
	4	$[0/90/0_4/45/\text{-}45_2/45]_S$	638.3	67
	5	$[0_4/45/\text{-}45/45/\text{-}45/90/0]_S$	626.4	29
lin. filter	1	$[0_2/90/0_3/\text{-}45/45_2/\text{-}45]_S$	640.2	95
	2	$[0_3/\text{-}45/45_2/\text{-}45/90/0_2]_S$	674.1	40
	3	$[45/0_5/90/\text{-}45/45/\text{-}45]_S$	689.2	94
	4	$[90/0_5/45/\text{-}45/45/\text{-}45]_S$	648.2	98
	5	$[45/0_5/90/\text{-}45/45/\text{-}45]_S$	689.2	99

In Figure 9, the stress-strain curves and differences between failure mechanisms of the first and

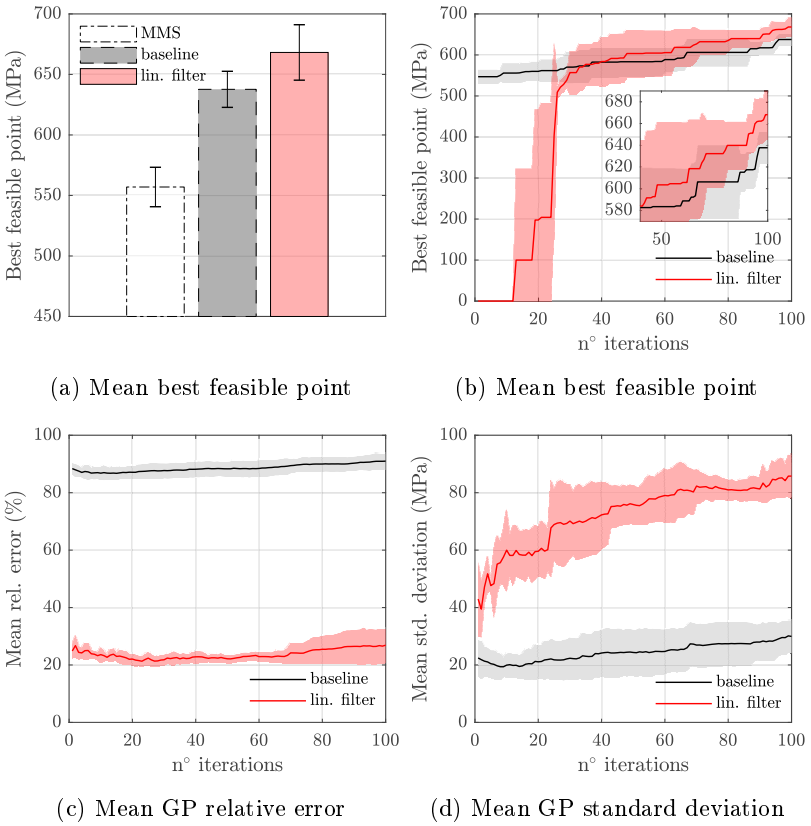

(a) Mean best feasible point

(b) Mean best feasible point

(c) Mean GP relative error

(d) Mean GP standard deviation

Figure 8: Optimisation results of case study I. In (a), comparison of mean best feasible point with baseline (no filtering) and linear filtering optimisation strategies, and with direct Maximin Sampling (MMS). In (b), progression of mean best feasible point, including zoom-in view. In (c), progression of the mean GP relative error. In (d), progression of the mean GP standard deviation. Each optimisation case is run five times. GP performance metrics are evaluated with an external dataset containing 500 points. In (b), (c) and (d), the mean values taken across all five repeat runs are plotted with solid lines and standard deviations with shaded areas.

final observed best feasible solutions obtained from optimisation lin. filter run n° 4 are shown. This particular example is used for conciseness, as the results are similar across different runs. The example is used to illustrate the differences in failure mechanisms of a non-optimised laminate and a final solution obtained from optimisation, and is not used for benchmarking purposes. The failure process is demonstrated at three strain states for each stacking sequence, and highlighted on the stress-strain curves. Transparency is added to the failure plots such that intralaminar cracking and delaminations (shaded areas) are visible through the laminate thickness.

5.2. Optimisation case study II: SA and NSA laminates

Considering the same 50/40/10 ply percentages, the feasible design space is now extended to include NSA laminates that match the in-plane stiffness. Using the methodology described in 3.5.1, a tolerance of $\epsilon_{\text{tol}} = 0.015$ and limiting solutions to a maximum of three angle pairs, the possible unique angle combinations for a 20-ply symmetric, balanced laminate are shown in Table 2. The feasible design space is now formed by the union of the solutions sets $\mathbf{V}_j$, each containing all unique permutations of the corresponding $\mathbf{v}_j$. Note that with a 5° discretisation of the design space, no

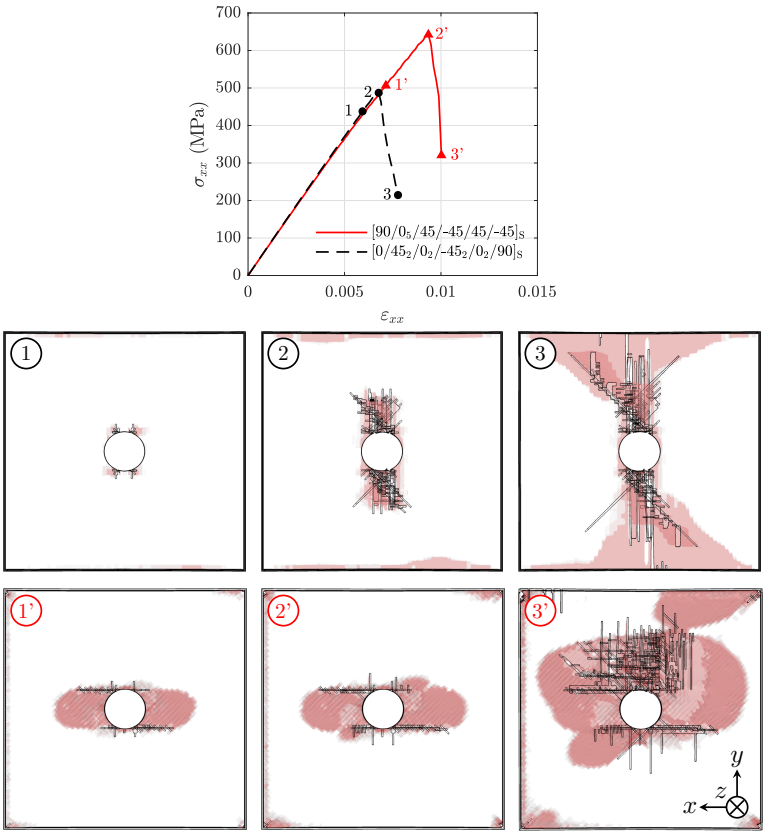

Figure 9: Comparison of stress-strain curves of first (non-optimised, in black) and final (in red) best observed feasible solutions obtained from case study I optimisation (lin. filter run n° 4 is used as an example). The failure process of each case is shown at three strain states, highlighted on the stress-strain curves. Loading applied in the x direction.

solutions exist within the specified tolerance for laminates with two angle pairs, and therefore, a 1° discretisation is used exceptionally for this particular case (corresponding to the angle combination $\mathbf{v}_2$ in Table 2).

The feasible design space is now much larger, representing a much more challenging optimisation problem. The feasible test set at each iteration $\mathcal{T}_f^i$ is generated following the method in section 3.5.2. The size of $\mathcal{T}_f^i$ is set to $F = 50000$, which is large enough to cover various feasible solutions, but still allows for very quick GP predictions. The optimisation results are shown in Figure 10, and are analogous to the comparative analysis shown for case study I in Figure 8. The best feasible stacking sequence from each optimisation run is displayed in Table 3 along its corresponding OHT strength and number of the iteration at which the solution is found.

5.3. Optimisation case study III: SA and NSA laminates with misaligned loading

Optimal stacking sequences for aerospace applications should be robust to uncertain loading and account for possible misalignments without resulting in significant knock-downs in strength. In this last case study, the optimisation of in-plane stiffness-matched SA and NSA laminates, considering the extended feasible design space of case study II, is performed for an applied misaligned load of

Table 2: Unique angle combinations for 20 ply symmetric, balanced laminate with 50/40/10 ply percentages, found from in-plane stiffness matching using the Monte Carlo method.

Unique angle combinations	**Lay-up**
$\mathbf{v}_1$	$[0_5/\pm 45_2/90]_S$
$\mathbf{v}_2$	$[\pm 10_3/\pm 57_2]_S$
$\mathbf{v}_3$	$[\pm 10_3/\pm 55/\pm 60]_S$
$\mathbf{v}_4$	$[\pm 10/\pm 25_3/\pm 80]_S$
$\mathbf{v}_5$	$[0_2/\pm 25_3/\pm 75]_S$
$\mathbf{v}_6$	$[\pm 10_2/\pm 30_2/\pm 75]_S$

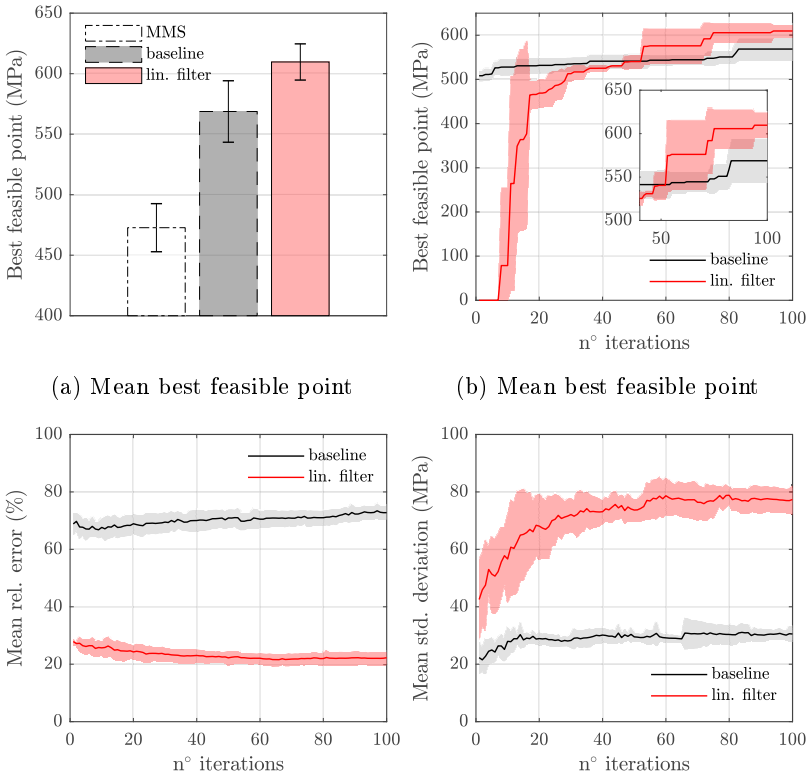

(a) Mean best feasible point

(b) Mean best feasible point

(c) Mean GP relative error

(d) Mean GP standard deviation

Figure 10: Optimisation results of case study II. In (a), comparison of mean best feasible point with baseline (no filtering) and linear filtering optimisation strategies, and with direct Maximin Sampling (MMS). In (b), progression of mean best feasible point, including zoom-in view. In (c), progression of the mean GP relative error. In (d), progression of the mean GP standard deviation. Each optimisation case is run five times. GP performance metrics are evaluated with an external dataset containing 500 points. In (b), (c) and (d), the mean values taken across all five repeat runs are plotted with solid lines and standard deviations with shaded areas.

10° instead of typical on-axis loading. To approximate the misaligned load, the FE model rotates the laminates by +10° and the load is applied in the same 0° axis, identical to the approach in [7].

The misalignment in load results in imbalance of plies about the loading axis and introduces extension-shear coupling, which can result in pronounced free edge effects. Thus, two optimisation cases are tested: (i) including the free edge effects (corresponding to the optimisation of a structure with exposed free edges); (ii) suppressing/reducing the free edge effects using the numerical edge treatment described in section 4 (approximating the case of a structure with no exposed free edges). Note that complete suppression of free edge effects with the numerical edge treatment in

Table 3: Best feasible solutions for each optimisation run in case study II. Stacking sequence, OHT strength and corresponding iteration at which the best feasible solution is found are shown.

Optimisation strategy	Run n°	Stacking sequence	OHT strength (MPa)	Iteration
baseline	1	$[\text{-}45/45/\text{-}45/90/0_2/45/0_3]_S$	571.0	73
	2	$[\text{-}45/45_2/90/0_4/\text{-}45/0]_S$	559.4	8
	3	$[0_2/45/\text{-}45_2/90/0_3/45]_S$	594.6	83
	4	$[\text{-}10/10_2/55/10/\text{-}55/60/\text{-}60/\text{-}10_2]_S$	530.7	55
	5	$[0_2/\text{-}45/0_3/90/45/\text{-}45/45]_S$	588.1	82
lin. filter	1	$[45_2/\text{-}45/90/0_5/\text{-}45]_S$	608.8	53
	2	$[0_4/45/\text{-}45/45/\text{-}45/90/0]_S$	626.4	53
	3	$[0_3/90/0_2/45/\text{-}45/45/\text{-}45]_S$	619.3	72
	4	$[45_2/\text{-}45/90/0_5/\text{-}45]_S$	608.8	75
	5	$[0_2/\text{-}45/0_3/90/45/\text{-}45/45]_S$	588.1	94

not possible [7].

First, the mean best feasible solution across the five repeat runs of the optimisation with linear filtering strategy is compared against two benchmarks: the mean of the best overall set of solutions found for on-axis loading (solutions from case study I optimisation with linear filtering strategy) but subjected to misaligned loading; the mean best solution from direct MMS (analogous to previous case studies). The benchmarking results are shown in Figure 11 for both cases with and without treatment.

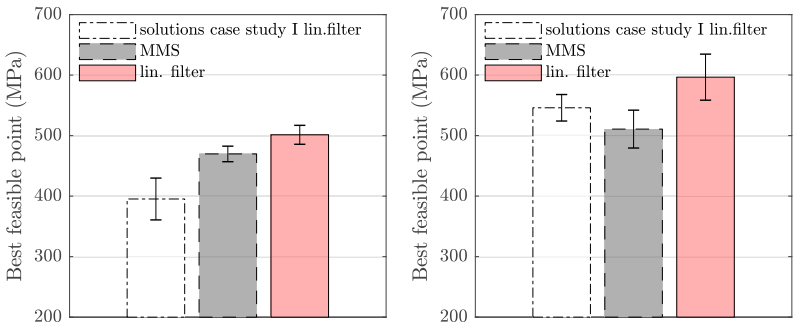

(a) Full free edge effects (b) Reduced free edge effects

Figure 11: Case study III benchmark, in (a) without numerical edge treatment (i.e exposed free edges) and in (b) with numerical edge treatment (i.e suppressed/reduced free edge effects). The mean best feasible point from linear filtering optimisation strategy is compared against the mean of best overall set of solutions found for on-axis loading (solutions from case study I with linear filtering optimisation strategy) but subjected to misaligned loading, and against direct Maximin Sampling (MMS).

The individual optimisation results for both cases with and without treatment are shown in Figure 12. For each case, the optimisation run yielding the best feasible solution is highlighted in black. The corresponding first and last observed best feasible solutions are highlighted with blue circle and red square markers, respectively. For clarity of Figure 12b, note that, in the highlighted case with numerical edge treatment, the first observed best feasible solution occurs at $i = 1$. The stress-strain curves of the solutions are displayed in the same colour as the corresponding

markers, and the failure patterns through the laminate thickness (including intralaminar cracking and delaminations) are shown at three strain states, highlighted on the stress-strain curves.

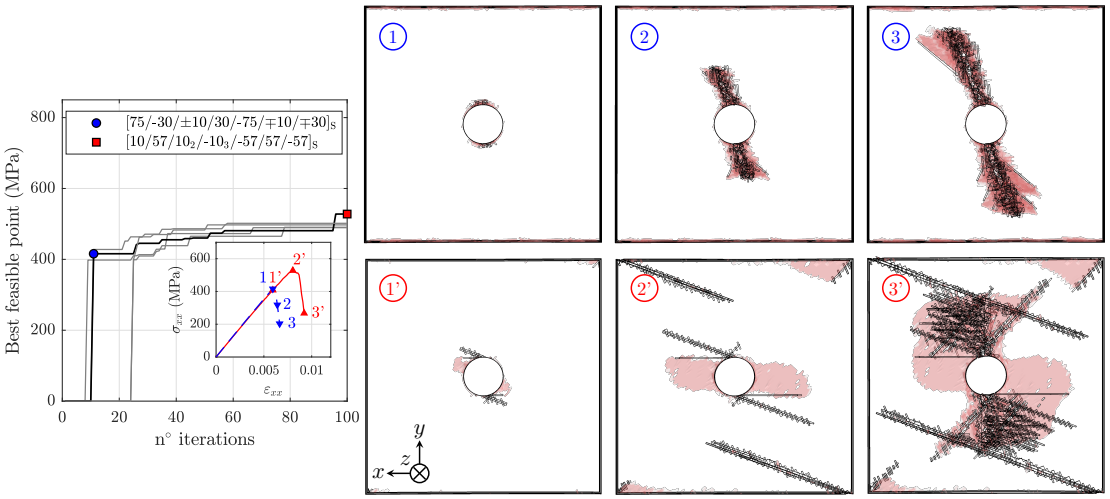

(a) Full free edge effects (structure with exposed free edges)

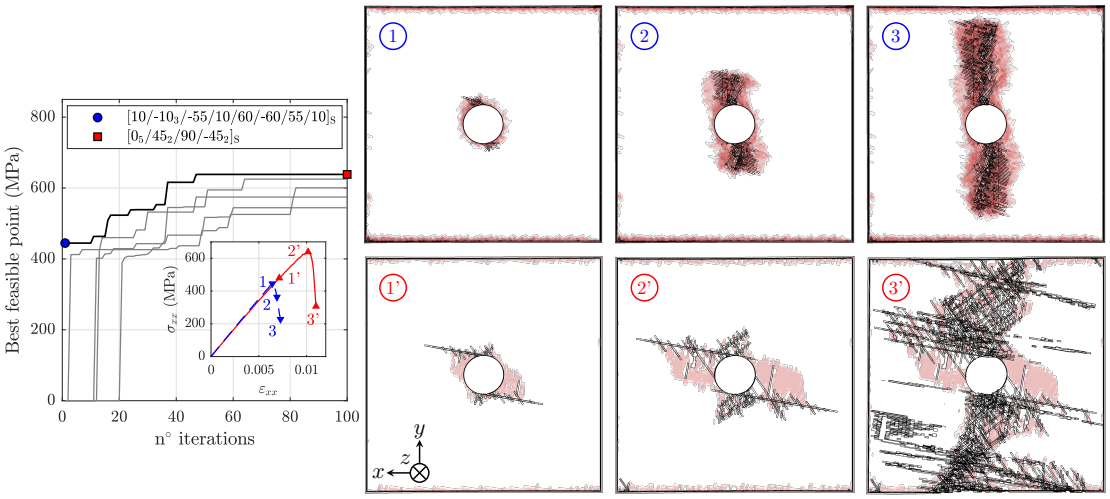

(b) Reduced free edge effects (approximate structure with no free edges)

Figure 12: Comparison of case study III optimisation runs: In (a) the OHT strength is predicted without numerical edge treatment (i.e with exposed free edges). In (b) the OHT strength is predicted with the numerical edge treatment (i.e with suppressed/reduced free edge effects). For each case, 5 optimisation runs were performed and the run resulting in the best observed feasible point is highlighted in black, with the first (blue circle) and last (red square) observed best feasible solutions highlighted with markers. The stress-strain curves of both first (in blue) and last (in red) best solutions are displayed and the failure patterns are shown at three strain states, highlighted on the stress-strain curves. Loading applied in the x direction.

The best feasible stacking sequence from each optimisation run, for both cases with and without numerical edge treatment, is displayed in Table 4.

6. Discussion

6.1. Comparison of Bayesian optimisation and direct sampling

The proposed Bayesian optimisation method returns significantly better solutions than direct MMS of feasible stacking sequences, after the same number of FE evaluations. This is first shown

Table 4: Best feasible solutions for each optimisation run in case study III. Stacking sequence, OHT strength and corresponding iteration at which the best feasible solution is found are shown.

Edge treatment	Run n°	Stacking sequence	OHT strength (MPa)	Iteration
No (Full free edge effects)	1	$[-60/10/55/-10/10_2/60/-10_2/-55]_S$	489.4	67
	2	$[10/-10_2/10_2/-10/-55/55/60/-60]_S$	490.5	78
	3	$[0/-45/90/0/45_2/0_3/-45]_S$	497.3	51
	4	$[10/57/10_2/-10_3/-57/57/-57]_S$	527.8	96
	5	$[0_2/-45/90/0/45/0/45/0/-45]_S$	501.7	58
Yes (Reduced free edge effects)	1	$[-45/45/-45/90/0_5/45]_S$	625.1	64
	2	$[90/-45_2/45/0_5/45]_S$	600.5	82
	3	$[10_3/-10_3/55/-60/60/-55]_S$	574.5	47
	4	$[-10_2/57/-57_2/-10/10/57/10_2]_S$	544.4	60
	5	$[0_5/45_2/90/-45_2]_S$	638.4	47

in case study I, in Figure 8a, where the baseline and the linear filtering optimisation strategies result in stacking sequences with, on average, 15% and 20% higher relative OHT strengths than the best MMS solution, respectively. The advantage of the optimisation strategies over MMS becomes even more significant in case study II, as shown in Figure 10a, where the baseline and linear filtering optimisation strategies return stacking sequences with, on average, 20% and 29% higher relative OHT strengths than the best MMS solution, respectively. This advantage is more pronounced in case study II due to the increased feasible design space, which makes it harder to reach a good feasible solution purely with random sampling methods. Note that in absolute values, the best observed solutions obtained in case study II display lower OHT strength than in case study I. This is expected, as SA laminates typically display higher OHT strengths under on-axis loading [7] and the inclusion of such a large number of NSA feasible stacking sequences in case study II makes it much more difficult to find good solutions, especially given the very limited number of iterations. The linear filtering optimisation strategy in case study III, in Figure 11, also displays better solutions than MMS, corresponding to 7% and 17% higher relative OHT strengths for the cases of exposed free edges (full free edge effects) and suppressed/reduced free edge effects, respectively. The benefits from optimisation are less pronounced for the case of misaligned loading, particularly for a structure with exposed free edges where OHT strength is very uniform across the feasible design space. For the case of misaligned loading with reduced free edge effects, the variability in OHT strength is, on the other hand, very large and thus, the optimisation would benefit from more iterations.

In addition, it can be observed from Figures 8b and 10b that the optimisation (considering both baseline and linear filtering strategies) only takes, at worst, an average of 40 iterations (55 FE evaluations) to match the mean of the best MMS solutions (115 FE evaluations) in case study I, and, similarly, only takes an average of 20 iterations (35 FE evaluations) in case study II. In case study III, the optimisation takes an average of 25 iterations (40 FE evaluations) for the case of exposed free edges in Figure 12a, and an average of 21 iterations (36 FE evaluations) for the

case of reduced free edge effects in Figure 12b, to match the mean of the best MMS solutions (115 FE evaluations). As such, the optimisation framework not only finds stronger solutions, but it also reaches the best solution from MMS within a fraction of the time in every case study. It is worth noting that although the global optimum is not achieved within 100 iterations in any of the case studies (resulting in different final solutions across the five repeat runs), the aim is to find the best possible solution in a fixed number of iterations given the complexity of the FE model, for which the framework is demonstrably successful.

6.2. Comparison of baseline and linear filtering optimisation strategies

The linear filtering strategy yields consistently better results than the baseline in both case studies I and II. Note, however, that the baseline optimisation with no filtering strategy displays feasible solutions at the first optimisation iterations, as shown in Figures 8b and 10b, as the initial training set contains feasible points only. The process takes longer to reach any observed feasible solution using the linear filtering strategy, because points are sampled from the whole design space. As the linear filter enforces the design constraints, the probability of sampling a feasible point increases.

Despite taking longer, sampling infeasible points in the initial training set and at the early stages of the process benefits the optimisation. As shown in Figures 8b and 10b, after an average of 40 iterations in case study I, and 47 iterations in case study II, the optimisation employing linear filtering reaches the mean best feasible point of the baseline and proceeds to find better mean feasible solutions than the baseline at every iteration until the end of the process.

The better performance of the linear filtering strategy is attributed to two factors: the much better accuracy of the GP; but also the increased uncertainty in GP predictions. The first factor is illustrated in Figures 8c and 10c for case studies I and II, respectively, where the linear filtering strategy displays a much lower mean relative error than the baseline. The high relative errors of the baseline optimisation indicate that feasible data is very restrictive, and that training must include infeasible points for the GP to more accurately capture the global trends in OHT strength. Note that the initial training set used in the linear filtering strategy provides most of the necessary training data. The effects of new sampled data on GP accuracy decrease as the linear filter enforces the design constraints, slightly decreasing the error until the test set becomes restricted to feasible solutions only. Then, because the feasible set is not representative of the whole design space, and thus very dissimilar to the 500-point external set where the mean GP relative error is computed, this error can increase slightly at later stages of the optimisation process, where the training data becomes more populated with points from the feasible set. Additionally, the error can increase as the GP is fitted to more data points near a local optimum (neglecting other areas of the design space), indicative of convergence or a focus upon exploitation rather than exploration. This trend can be observed in case study I after 70 iterations, in Figure 8c. In case study II, the mean relative error remains constant with increasing feasible training data due to the large size of the feasible

design space, which is more representative of the whole space. This larger feasible space also explains why the mean relative error of the baseline strategy is lower in case study II than in case study I.

The second factor is demonstrated in both Figures 8d and 10d, where the linear filtering strategy displays higher mean GP standard deviations than the baseline. This increased uncertainty leads to a more explorative optimisation process, which is particularly important in problems with large feasible design spaces such as case study II. The baseline strategy, on the other hand, is more likely to exploit solutions near best observed feasible points and more likely to converge to local maxima, rather than exploring areas of the feasible design space where the objective function value is unknown. The higher mean GP standard deviations of the linear filtering strategy can be attributed to the fact that during the early optimisation stages, the GP is fitted to points with larger variations in OHT strength due to the space-filling test set. The rate of increase in mean GP standard deviation diminishes once the test set is filtered to feasible solutions only, where OHT strength is less variable. The baseline strategy, on the other hand, is exposed to little variation in OHT strength due to the very limited test set and thus, displays much lower mean GP standard deviation across the 500-point external validation set. The higher GP standard deviation in the linear filtering strategy therefore reflects a more realistic approximation of the underlying global trends, in which significant variations in strength can occur.

As a final remark, it should be noted that the improvement from using the linear filtering strategy over the baseline is greater in case study II, representing a 7.2% relative increase in average OHT strength at the end of the optimisation process, compared to 4.8% in case study I. This greater relative improvement demonstrates the benefits of the filtering strategy when dealing with design spaces comprised of more feasible solutions, which are inherently more difficult to search and to find points with highest performance. These benefits are anticipated to be even greater for problems with even larger sets of feasible solutions. For such cases, the baseline strategy is particularly ineffective, as its combination of poor GP accuracy and low uncertainty is more likely to result in convergence to solutions mistaken for optima.

6.3. Drawing laminate design guidelines using the Bayesian optimisation framework

Deriving physical intuition and establishing good and bad design practices for the strength of a particular structure generally requires multiple observations across the design space, selected by the designer. The proposed Bayesian optimisation framework can be used as a pragmatic tool to efficiently navigate the design space and understand design principles from a small number of observations. The cases of on-axis loading (in case study I and II) and misaligned loading (in case study III) are investigated as illustrative examples of the framework as a tool to establish design guidelines.

6.3.1. On-axis loading

For OHT strength of laminates under on-axis loading, the best feasible solutions from optimisation correspond to SA laminates with significant 0° ply blocking, as shown in Tables 1 and 3. As detailed in [6, 7], blocking of 0° plies leads to shearing of the matrix resulting in cracks tangential to the hole that reduce fibre stresses and delay fibre failure. On the other hand, fibre failure tends to occur earlier in dispersed SA laminates. The difference in failure type can be observed in Figure 9, where the optimised stacking sequence containing a thick block of 0_5 plies displays extensive sub-critical matrix shear cracks in the 0° direction, resulting in more progressive failure. As a result, at ultimate failure, the optimised stacking sequence is able to accumulate more visible damage than the non-optimised (dispersed) one. Despite the lack of physical intuition, the GP can efficiently establish correlations between ply block thickness and OHT strength, driving the optimisation process towards areas of the design space with SA stacking sequences comprising thick blocks of 0° plies and avoiding excessively dispersed laminates. Similarly, despite the significantly larger feasible design space and much more challenging optimisation problem in case study II, the GP is generally able to drive the optimisation towards blocked SA laminates within the specified maximum number of iterations, avoiding both NSA and dispersed SA laminates due to their lower OHT strength (only with the exception of baseline run n° 4, as can be observed in Table 3).

6.3.2. Misaligned loading

Under misaligned loading, optimal stacking sequences and the direction of optimisation greatly depend on whether the structure has exposed free edges or whether these are suppressed/reduced in the FE model with the numerical edge treatment, replicating the conditions in a structure with no exposed free edges.

As shown in Table 4, the consideration of exposed free edges leads to solutions consisting of mainly NSA laminates and more dispersed SA laminates, with the highest observed OHT strength corresponding to the NSA stacking sequence $[10/57/10_2/\text{-}10_3/\text{-}57/57/\text{-}57]_S$. The best observed stacking sequences in the edge treated cases, on the other hand, correspond to SA laminates with very blocked 0° plies. As such, from Figure 11, it can be observed that the best set of on-axis solutions (corresponding to the linear filtering optimisation strategy in case I study), also displaying thick blocks of 0° plies, are much more robust to misaligned loading when free edge effects are suppressed than when they are exposed.

It can be observed from both Figures 12a and 12b that, analogous to on-axis loading, the best solutions in either cases with or without edge treatment display much more extensive sub-critical intralaminar matrix cracking than corresponding non-optimised solutions. Note that the improvements from optimisation are greater in the edge treated case. This is because the reduced free edge effects prevent premature growth of critical intralaminar cracks that grow from the free edges, which tends to predominantly affect stacking sequences (such SA laminates with 0° ply blocking) which are also prone to beneficial sub-critical matrix cracking at the hole. Without

edge treatment, these stacking sequences fail much earlier than NSA and dispersed SA laminates. Conversely, by applying the edge treatment, matrix cracking localises at the hole and delays fibre failure, explaining why the best on-axis solutions are much more robust to misaligned loading when free edge effects are suppressed.

Despite corresponding to essentially the same optimisation problem, with an identical feasible design space and loading condition, the consideration of a structure with or without exposed free edges results in significantly different optimal stacking sequences. The GP is able to efficiently drive the optimisation process accordingly, directing the search towards regions of optimal solutions without explicit information on the effects of free edges on the failure mechanisms. More importantly, the example illustrates how the optimisation framework can be used to aid in establishing laminate design guidelines in structures under different conditions, whilst providing insight into the physical mechanisms that justify those guidelines.

7. Conclusions

A novel Bayesian optimisation framework is proposed for the design and stacking sequence selection of stronger composite laminates. The framework is the first to combine a novel data-driven optimisation methodology with high-fidelity, meso-scale progressive damage finite element modelling. Gaussian process regression is used as a surrogate for the computationally expensive FE model. The latter is only evaluated at solutions that are expected to yield an improvement in the optimisation routine. A laminate subjected to open-hole tension was used as an example problem and the strength was optimised considering other design requirements, such as specified in-plane stiffness, corresponding to that of a wing skin, balance of plies and symmetry about the laminate mid-plane. In order to cope with the very restricted design space due to the imposed constraints, the framework includes a bespoke filtering strategy. This methodology allows sampling of infeasible solutions at the early stages of the optimisation to improve the performance of the surrogate model, and gradually enforces the design constraints as the optimisation progresses, directing the search towards optimal feasible regions.

The advantages of the framework and the proposed filtering strategy were demonstrated using three case studies, considering both standard and non-standard ply angles, aligned and misaligned loading, and full or reduced free edge effects. With the linear filtering strategy, the optimisation reaches consistently better solutions, corresponding, on average, up to 29% greater OHT strength than direct sampling of feasible stacking sequences using MMS and 7.2% greater OHT strength than the optimisation without filtering strategy (baseline). The proposed optimisation framework not only finds stronger solutions, but it also reaches the best solution obtained from MMS within a fraction of the time in every case study (on average 48% of MMS runtime at worst, and 30% at best), representing potential savings in computation runtime.

The case studies also demonstrate the potential of the optimisation framework as a tool to

quickly establish preliminary design principles. The framework shows that for on-axis loading, and misaligned loading in structures with no exposed free edges, SA laminates with significant 0° ply blocking provide the highest OHT strengths. However, for structures with exposed free edges and under misaligned loading, dispersed SA and NSA laminates generally provide the highest strengths.

The presented case studies therefore illustrate in a general sense how the proposed framework may be used to find relatively high-performance, unconventional laminates incorporating non-standard angles, in instances wherein global optimisation methods are intractable, due to computationally expensive governing FE models and in which the feasible regions are heavily constrained by industrial design requirements.

8. Acknowledgements

T.R.C. Chuaqui is funded by GKN Aerospace and EPSRC, United Kingdom. C. Scarth, A.T. Rhead and R. Butler are supported by EPSRC research grant Certification for Design - Reshaping the Test Pyramid (CerTest, EP/S017038/1). R. Butler holds a Royal Academy of Engineering/GKN Aerospace Research Chair.

References

[1] S. Abrate. Optimal design of laminated plates and shells. *Composite Structures*, 29:269–286, 1994.

[2] H. Ghiasi, D. Pasini, and L. Lessard. Optimum stacking sequence design of composite materials Part I: Constant stiffness design. *Composite Structures*, 90(1):1–11, 2009.

[3] S. W. Tsai, S. Sihn, J. D. D. Melo, A. Arteiro, and R. Rainsberger. Composite Laminates theory and practice of analysis, design and automated layup. In *Composite Laminates theory and practice of analysis, design and automated layup*, pages 113–185. Stanford Aeronautics & Astronautics, 2017.

[4] K. J. Johnson, R. Butler, E. G. Loukaides, C. Scarth, and A. T. Rhead. Stacking sequence selection for defect-free forming of uni-directional ply laminates. *Composites Science and Technology*, 171:34–43, 2019.

[5] S. Shrivastava, N. Sharma, S. W. Tsai, and P. M. Mohite. D and DD-drop layup optimization of aircraft wing panels under multi-load case design environment. *Composite Structures*, 248(May):112518, 2020.

[6] S. R. Hallett, B. G. Green, W. Jiang, K. H. Cheung, and M. R. Wisnom. The open hole tensile test: a challenge for virtual testing of composites. *International Journal of Fracture*, 158:169–181, 2009.

[7] T. R. C. Chuaqui, M. W. D. Nielsen, J. Colton, R. Butler, and A. T. Rhead. Effects of ply angle and blocking on open-hole tensile strength of composite laminates: A design and certification perspective. *Composites Part B*, 207(June 2020):108582, 2021.

[8] K. Yamaguchi, S. E. Phenisee, Z. Chen, M. Salviato, and J. Yang. Ply-drop design of non-conventional laminated composites using Bayesian optimization. *Composites Part A*, 139(October):106136, 2020.

[9] J. Bergstra, R. Bardenet, Y. Bengio, and B. Kégl. Algorithms for hyper-parameter optimization. In *Advances in Neural Information Processing Systems*, pages 2546–2554, 2011.

[10] J. Snoek, H. Larochelle, and R. P. Adams. Practical Bayesian optimization of machine learning algorithms. In *Advances in Neural Information Processing Systems*, pages 2951–2959, 2012.

[11] C. Thornton, F. Hutter, H. H. Hoos, and K. Leyton-Brown. Auto-WEKA: Combined selection and hyperparameter optimization of classification algorithms. In *Knowledge Discovery and Data Mining*, pages 847–855, 2013.

[12] K. Swersky, J. Snoek, and R. P. Adams. Multi-task Bayesian optimization. In *Advances in Neural Information Processing Systems*, pages 2004–2012, 2013.

[13] E. Brochu, V. M. Cora, and N. de Freitas. A tutorial on Bayesian optimization of expensive cost functions, with application to active user modeling and hierarchical reinforcement learning. Technical report, Dept. of Computer Science, University of British Columbia, 2009.

[14] D. Lizotte, T. Wang, M. Bowling, and D. Schuurmans. Automatic gait optimization with Gaussian process regression. In *IJCAI*, pages 944–949, 2007.

[15] R. Martinez-Cantin, N. de Freitas, A. Doucet, and J. A. Castellanos. Active policy learning for robot planning and exploration under uncertainty. In *Robotics Science and Systems*, 2007.

[16] R. Marchant and F. Ramos. Bayesian optimisation for intelligent environmental monitoring. In *NIPS workshop on Bayesian Optimization and Decision Making*, 2012.

[17] A. Solomou, G. Zhao, S. Boluki, J. K. Joy, X. Qian, I. Karaman, R. Arróyave, and D. C. Lagoudas. Multi-objective Bayesian materials discovery: Application on the discovery of precipitation strengthened NiTi shape memory alloys through micromechanical modeling. *Materials & Design*, 160:810–827, 2018.

[18] S. Sano, T. Kadowaki, K. Tsuda, and S. Kimura. Application of Bayesian Optimization for Pharmaceutical Product Development. *Journal of Pharmaceutical Innovation*, 15:333–343, 2020.

[19] B. Shahriari, K. Swersky, Z. Wang, R. P. Adams, and N. de Freitas. Taking the Human Out of the Loop : A Review of Bayesian Optimization. In *IEEE*, number 1, pages 1–24, 2016.

[20] M. A. Bessa and S. Pellegrino. Design of ultra-thin shell structures in the stochastic post-buckling range using Bayesian machine learning and optimization. *International Journal of Solids and Structures*, 139-140:174–188, 2018.

[21] Qi Guo, Jiutao Hang, Suian Wang, Wenzhi Hui, and Zonghong Xie. Buckling optimization of variable stiffness composite cylinders by using multi-fidelity surrogate models. *Thin-Walled Structures*, 156:107014, nov 2020.

[22] Qi Guo, Jiutao Hang, Suian Wang, Wenzhi Hui, and Zonghong Xie. Design optimization of variable stiffness composites by using multi-fidelity surrogate models. *Structural and Multidisciplinary Optimization*, 63(1):439–461, jan 2021.

[23] Jifan Zhong, Yaochen Zheng, Jianqiao Chen, and Zhao Jing. Variable-stiffness composite cylinder design under combined loadings by using the improved Kriging model. *Acta Mechanica Sinica*, 35(1):201–211, feb 2019.

[24] A. G. Passos, M. A. Luersen, and C. A. Steeves. Optimal curved fibre orientations of a composite panel with cutout for improved buckling load using the Efficient Global Optimization algorithm. *Engineering Optimization*, 49(8):1354–1372, aug 2017.

[25] Weifei Hu, Wentao Zhao, Yeqing Wang, Zhenyu Liu, Jin Cheng, and Jianrong Tan. Design optimization of composite wind turbine blades considering tortuous lightning strike and non-proportional multi-axial fatigue damage. *Engineering Optimization*, 52(11):1868–1886, nov 2020.

[26] Homero Valladares and Andres Tovar. Design Optimization of Sandwich Composite Armors for Blast Mitigation Using Bayesian Optimization with Single and Multi-Fidelity Data. apr 2020.

[27] J. M. Finley, M. S. P. Shaffer, and S. Pimenta. Data-driven intelligent optimisation of discontinuous composites. *Composite Structures*, 243(February):112176, 2020.

[28] Adriana W. Blom, Patrick B. Stickler, and Zafer Gürdal. Optimization of a composite cylinder under bending by tailoring stiffness properties in circumferential direction. *Composites Part B: Engineering*, 41(2):157–165, mar 2010.

[29] Zhouzhou Pan, Lu-Wen Zhang, and K.M. Liew. Adaptive surrogate-based harmony search algorithm for design optimization of variable stiffness composite materials. *Computer Methods in Applied Mechanics and Engineering*, 379:113754, jun 2021.

[30] Zhihua Wang, José Humberto S. Almeida Jr., Luc St-Pierre, Zhonglai Wang, and Saullo G.P. Castro. Reliability-based buckling optimization with an accelerated Kriging metamodel for filament-wound variable angle tow composite cylinders. *Composite Structures*, 254:112821, dec 2020.

[31] C. E. Rasmussen and C. K. I. Williams. *Gaussian Processes for Machine Learning*. The MIT Press, 2006.

[32] H. Moon, A. Dean, and T. Santner. Algorithms for Generating Maximin Latin Hypercube and Orthogonal Designs. *Journal of Statistical Theory and Practice*, 5(1):81–98, 2011.

[33] J. Nocedal and S. J. Wright. *Numerical Optimization*. Springer Series in Operations Research, Springer Verlag, second edi edition, 2006.

[34] Nicholas Metropolis, Arianna W. Rosenbluth, Marshall N. Rosenbluth, Augusta H. Teller, and Edward Teller. Equation of State Calculations by Fast Computing Machines. *The Journal of Chemical Physics*, 21(6):1087–1092, jun 1953.

[35] R. M. Neal. Monte Carlo Implementation of Gaussian Process Models for Bayesian Regression and Classification. Technical report, University of Toronto, 1997.

[36] D. R. Jones, M. Schonlau, and W. J. Welch. Efficient Global Optimization of Expensive Black-Box Functions. *Journal of Global Optimization*, 13:455–492, 1998.

[37] S. W. Tsai, J. C. Halpin, and N. J. Pagano. Invariant Properties of Composite Materials. In *Composite materials workshop*, pages 233–253. Stanford CT: Technomic Publishing Co., Inc.

[38] M. Miki and Y. Sugiyamaf. Optimum Design of Laminated Composite Plates Using Lamination Parameters. *AIAA Journal*, 31(5):921–922, 1993.

[39] Jacob R. Gardner, Matt J. Kusner, Zhixiang Xu, Kilian Q. Weinberger, and John P. Cunningham. Bayesian optimization with inequality constraints. *31st International Conference on Machine Learning, ICML 2014*, 3:2581–2591, 2014.

[40] ABAQUS Documentation. Dassault Systèmes Simulia Corp, Providence, RI.

[41] T. A. Fletcher, T. Kim, T. J. Dodwell, R. Butler, R. Scheichl, and R. Newley. Resin treatment of free edges to aid certification of through thickness laminate strength. *Composite Structures*, 146:26–33, 2016.

[42] T. R. C. Chuaqui, E. Sebastian, V. Sahadevan, A. T. Rhead, and R. Butler. Edge treatment of short beam shear tests for improved assessment of structural strength. *Composites Part A: Applied Science and Manufacturing*, 137(105991), 2020.

[43] P. Maimí, P. P. Camanho, J. A. Mayugo, and C. G. Dávila. A continuum damage model for composite laminates: Part I - Constitutive model. *Mechanics of Materials*, 39:897–908, 2007.

[44] P. Maimí, P. P. Camanho, J. A. Mayugo, and C. G. Dávila. A continuum damage model for composite laminates: Part II - Computational implementation and validation. *Mechanics of Materials*, 39:909–919, 2007.

[45] E. Martín-Santos, P. Maimí, E.V. González, and P. Cruz. A continuum constitutive model for the simulation of fabric-reinforced composites. *Composite Structures*, 111:122–129, may 2014.

[46] P.P. Camanho, P. Maimí, and C.G. Dávila. Prediction of size effects in notched laminates using continuum damage mechanics. *Composites Science and Technology*, 67(13):2715–2727, oct 2007.

[47] Masaru Zako and Yasutomo Uetsuji. On the Damage Behavior of Fiber Reinforced Composite Materials. *International Journal of Damage Mechanics*, 11(2):187–202, apr 2002.

[48] M.V. Donadon, L. Iannucci, B.G. Falzon, J.M. Hodgkinson, and S.F.M. de Almeida. A progressive failure model for composite laminates subjected to low velocity impact damage. *Computers & Structures*, 86(11-12):1232–1252, jun 2008.

[49] T. A. Bogetti, C. P. R. Hoppel, V. M. Harik, J. F. Newill, and B. P. Burns. Predicting the nonlinear response and progressive failure of composite laminates. *Composites Science and Technology*, 64:329–342, 2004.

[50] T. A. Bogetti, C. P. R. Hoppel, V. M. Harik, J. F. Newill, and B. P. Burns. Predicting the nonlinear response and failure of composite laminates: correlation with experimental results. *Composites Science and Technology*, 64:477–485, 2004.

[51] P. P. Camanho, C. G. Dávila, S. T. Pinho, L. Iannucci, and P. Robinson. Prediction of in situ strengths and matrix cracking in composites under transverse tension and in-plane shear. *Composites Part A: Applied Science and Manufacturing*, 37:165–176, 2006.

[52] O. Falcó, R. L. Ávila, B. Tijs, and C. S. Lopes. Modelling and simulation methodology for unidirectional composite laminates in a Virtual Test Lab framework. *Composite Structures*, 190:137–159, 2018.